J. Fluid Mech. (1986), *vol.* 170, *pp.* 113–137
Printed in Great Britain

The role of wave-induced pressure fluctuations in the transfer processes across an air–water interface

By YIANNIS ALEX PAPADIMITRAKIS†, EN YUN HSU AND ROBERT L. STREET

Environmental Fluid Mechanics Laboratory, Department of Civil Engineering, Stanford University, Stanford, California 94305

(Received 1 June 1983 and in revised form 20 February 1986)

The structure of the pressure and velocity fields in the air above mechanically generated water waves was investigated in order to evaluate their contribution to the transfer of momentum and energy from wind to water waves. The measurements were taken in a transformed Eulerian wave-following frame of reference, in a wind-wave research facility at Stanford University.

The organized component of the fluctuating static pressure at the channel roof was found to contain contributions from both the sound field and the reflected water wave. The acoustic contributions were accounted for by appropriately correcting the pressure amplitude and phase (relative to the wave) and its contribution to the momentum and energy exchange. The wave-induced pressure coefficient at the fundamental mode shows in general an exponential decay behaviour with height, but the rate of decay is different from that predicted by potential-flow theory. The wave-induced pressure phase relative to the wave remains fairly constant throughout the boundary layer, except when the ratio of the wave speed to the freestream velocity, $c/U_{\delta_0} = 0.78$ and 0.68. This phase difference was found to be about 130° during active wave generation, with the pressure lagging the wave. The momentum and energy transfer rates supported by the waves were found to be dominated by the wave-induced pressure, but the transfer of the corresponding total quantities to both waves and currents may or may not be so dominated, depending on the ratio c/U_{δ_0}. The direct contribution of the wave-induced Reynolds stresses to the transfer processes is negligible.

1. Introduction

In the theory of water-wave generation by wind, the wave-induced pressure appears to play a significant role in the momentum and energy exchange. Experimental observations of the wave-induced pressure in the turbulent boundary layer above water waves are limited and have been confined either to the water surface or at a short distance above the crests of laboratory or sea waves. Such past measurements (Shemdin & Hsu 1967; Yu, Hsu & Street 1973; Wu, Hsu & Street 1979; Dobson 1971; Elliott 1972*b*; Snyder 1974) were inconsistent among themselves and in disagreement with Miles' (1957) theory. The joint field measurements of Snyder *et al.* (1981) partially removed the discrepancy among previous measurements and gave a consistent picture of the pressure profile over a limited range of dimensionless height and wind speeds. It is now known that Dobson's (1971) value of the growth rate factor

† Present address: College of Marine Studies, University of Delaware, Newark, DE 19716.

β is too high by a factor of three; the Snyder *et al.* (1981) pressure measurements are thought to be closest to correct.

In this study, Eulerian wave-following measurements of the fluctuating static pressure in the air boundary layer over 1 Hz, 2.54 cm nominal amplitude, mechanically generated water waves were taken in the Stanford wind/water-wave research facility. Simultaneous measurements of the air velocity and the wave height were also taken in order to evaluate the contribution of the wave-induced pressure and other mechanisms to the momentum and energy exchange.

Although it is difficult to simulate 'typical' sea states in a laboratory, and the legitimacy of comparing field and laboratory data is questionable, the presence of mechanically generated water waves makes the laboratory and oceanic conditions governing the transfer processes both physically and dynamically similar and therefore also makes the corresponding results comparable (Phillips 1977, p. 129). Furthermore, because ocean waves are usually random and three-dimensional instead of organized and two-dimensional, as Miles (1957) assumed, it has always seemed likely that laboratory data obtained from flows over mechanically generated waves would produce a more convincing test of Miles' (1957) theory (we learn differently in this case; cf. §4.1). For the above reasons, sinusoidal water waves were selected for this investigation. Because of the simplicity of the wave form, the characteristics of the wave-induced perturbations can be easily extracted. However, laboratory measurements of the wave-induced pressure above water waves are difficult to make and may be different from those in the field for various reasons, the most important being: (i) the small magnitude of pressure fluctuations; (ii) the pressure contamination from dynamic noise, mechanical vibrations, acoustic and water-wave reflection effects; (iii) the presence of bound components.

The pressure and velocity fields were measured here with a specially designed high-sensitivity pressure instrument and two X hot films mounted on a wave-following device. An array of five piezocrystal pressure transducers mounted flush with the channel roof was also used to resolve the organized spurious pressure components associated with the sound field and the reflected water wave. The water-wave characteristics were obtained with the aid of two wave-height gauges, one of which drove the wave-following device. This paper describes the structure of the wave-induced pressure field obtained in the Eulerian wave-following frame and its contribution to the momentum and energy transfer process across the air–water interface.

2. Theoretical background

2.1. *Basic ideas*

In this study we consider a turbulent channel flow of air above a progressive sinusoidal water wave with a small amplitude a (i.e. wave slope $\leqslant 0.1$) and a frequency ω. Thus the instantaneous signal $g(\boldsymbol{x}, t)$ in the air stream will be decomposed into three different components, viz. $g(\boldsymbol{x},t) = \bar{g}(\boldsymbol{x})+\tilde{g}(\boldsymbol{x},t)+g'(\boldsymbol{x},t)$, representing respectively the time-independent mean, the wave-induced flow, and turbulent motions. Here $\boldsymbol{x}$ represents the position (vector) where the quantity $g(\boldsymbol{x}, t)$ is measured and t is the time. Familiar time (overbar) and phase (brackets) averages are used, so $\tilde{g}(\boldsymbol{x},t) = \langle g(\boldsymbol{x},t)\rangle - \bar{g}(\boldsymbol{x})$.

The general two-dimensionality of the flow regime above wind-generated waves in our facility was established through a series of tests described by E. Y. Hsu (1965). In the presence of long mechanically generated waves with small slope, we anticipate the air flow to be even more two-dimensional for the same wind speed, as the long

waves reduce ripple production through the Phillips & Banner (1974) mechanism and minimize short-wave three-dimensional effects. Furthermore, according to Garret (1970), cross-water waves cannot be generated in our tank because its width (0.9 m) is much smaller than the length of the primary wave being generated by the wave-maker (1.55 m). It is therefore highly unlikely that ripples can be involved, in some catalytic way, in the transfer processes. The two-dimensional character of the mechanically generated sinusoidal wave was checked with the aid of two wave-height gauges placed across the channel at the same fetch and at different stations. Both the air- and the water-wave fields can be considered as two-dimensional.

In the Cartesian coordinate system used, x is measured in the direction of wave propagation, with its origin at the equilibrium position of the wavemaker, y is the vertical coordinate measured upward from the mean water level (MWL), and z is the lateral coordinate parallel to the wave front. The simple wave-following coordinate transformation used by Hsu, Hsu & Street (1981) is used here as well, viz.

$$t = t^*, \quad x = x^*, \quad y = y^* + f(y^*)\,\tilde{\eta}, \quad z = z^*, \tag{2.1a, b, c, d}$$

$$f(y^*) = \frac{\sinh(kH - ky^*)}{\sinh(kH)}, \tag{2.2}$$

where $\tilde{\eta}$ represents the sinusoidal water-surface displacement from the MWL and H (= 1.07 m) is the depth of the air flow measured from the MWL to the channel roof. Then we write

$$\tilde{\eta} = a_{\mathrm{I}} \cos(kx - \omega t + \theta'_{\mathrm{I}}) + a_{\mathrm{R}} \cos(kx + \omega t + \theta'_{\mathrm{R}}) + a_{\mathrm{B2}} \cos(2kx - 2\omega t + \theta'_{\mathrm{B2}}) + a_{\mathrm{F2}} \cos(k_2 x - 2\omega t + \theta'_{\mathrm{F2}}) + \text{higher harmonics}. \tag{2.3}$$

a_{I} and a_{R} are the amplitudes of the primary incident and reflected waves, while a_{B2} and a_{F2} are the amplitudes of a bound and a free second harmonic; θ'_{I}, θ'_{R}, θ'_{B2} and θ'_{F2} are the corresponding phase lags and k, k_2 are wavenumbers obeying the following approximate deep water-wave relationships:

$$\omega^2 = kg, \quad 4\omega^2 = k_2 g, \tag{2.4a, b}$$

where g is the gravitational acceleration. The properties of the transformation and the differences in physical significance for flow quantities obtained in a fixed and a wave-following frame of reference, according to (2.1*a–d*) and (2.2) were identified and critically examined by Hsu *et al.* (1981).

In (2.3) the surface wave has been described to second order as a Stokes second-order progressive wave, a free second harmonic, and the primary reflected wave (Madsen 1971). The incident wave may be slightly nonlinear. Lake & Yuen's (1978) condition that a wavetrain behaves as a nonlinear bound-wave system when the average wave slope exceeds about 0.1 is also satisfied in this study. Our measurements have shown that the reflection coefficient $\epsilon = a_{\mathrm{R}}/a_{\mathrm{I}}$ is approximately 5 % for the 1 Hz mechanically generated wave used in this study. Hence the reflected wave is of the same order of magnitude as the second-harmonic motion associated with the incident wave. The water surface-roughness condition depending on the roughness height $y_0 = (\overline{\eta'^2})^{\frac{1}{2}}$ and characterized by the roughness parameter $y_0^+ = y_0 u_*/\nu$ was found to vary from aerodynamically smooth to fully rough according to traditional measures (see Papadimitrakis, Hsu & Street 1984); here η' is the instantaneous ripple height, and u_* and ν are the friction velocity and kinematic viscosity of the air respectively.

In describing the wave perturbations, distinction should be made between the

velocity and pressure fields. Reflection effects appear to be significant only for the latter, as the perturbation pressure associated with the primary reflected wave, $\tilde{p}_{\mathrm{R}}$, can exceed the travelling downstream wave-induced pressure $\tilde{p}_{\mathrm{I}}$. Spectral analysis indicates that (in contrast with the small wave-induced velocity harmonics† found in this investigation, in Hsu *et al.* (1981) and Hsu & Hsu (1983)), the perturbation pressures appear to be significant at higher frequencies up to 5 Hz. Therefore, in studying the behaviour of $\tilde{u}$, $\tilde{v}$ and $\tilde{p}$ a focus about the fundamental wave mode is satisfactory for $\tilde{u}$ and $\tilde{v}$, but not for $\tilde{p}$. Consequently, attention was also given to the wave-induced pressure harmonics, up to 5 Hz. The form of all wave-induced pressure components and their treatment in spectral and other calculations in order to either deduce their amplitude and phase and/or their contribution to the momentum and energy exchange is further discussed in §3.2.

2.2. *Momentum and energy transfer-rate equations*

In order to evaluate the contribution of the wave-induced pressure to the momentum and energy exchange the transfer-rate equations were derived in the transformed coordinate system. The mean momentum and energy transfer rates, per unit horizontal area, supported by the waves and currents and evaluated at the edge of the viscous sublayer where the viscous stresses can be neglected, are as follows:

$$\overline{M}_{x^*\mathrm{w}} = \left[\overline{(\tilde{p}+\rho\tilde{r}_{11})\frac{\partial\tilde{\eta}}{\partial x^*}}\right]_{y^*=\delta_*}, \quad \overline{M}_{x^*\mathrm{c}} = [-\rho\overline{u'v'}]_{y^*=\delta_*}, \tag{2.5a, b}$$

$$\overline{M}_{y^*\mathrm{w}} = \left[-\rho\overline{\tilde{r}_{12}\frac{\partial\tilde{\eta}}{\partial x^*}}\right]_{y^*=\delta_*}, \quad M_{y^*\mathrm{c}} = [(P+\rho\overline{v'v'})]_{y^*=\delta_*}, \tag{2.6a, b}$$

$$\overline{M}_{\mathrm{w}} = \overline{M}_{x^*\mathrm{w}} + \overline{M}_{y^*\mathrm{w}}, \quad \overline{M}_{\mathrm{c}} = \overline{M}_{x^*\mathrm{c}} + \overline{M}_{y^*\mathrm{c}}, \tag{2.7a, b}$$

$$\overline{E}_{x^*\mathrm{w}} = \left[-\rho\overline{\tilde{r}_{12}\tilde{u}} + \rho(\overline{u'u'}-\overline{v'v'})\overline{\frac{\partial\tilde{\eta}}{\partial x^*}\tilde{u}}\right]_{y^*=\delta_*}, \tag{2.8}$$

$$\overline{E}_{y^*\mathrm{w}} = -\left[\overline{\tilde{p}\tilde{v}} + \rho\overline{\tilde{r}_{22}\tilde{v}} - \rho\overline{u'v'}\overline{\frac{\partial\tilde{\eta}}{\partial x^*}\tilde{v}}\right]_{y^*=\delta_*}, \tag{2.9}$$

$$\overline{E}_{\mathrm{w}} = \overline{E}_{x^*\mathrm{w}} + \overline{E}_{y^*\mathrm{w}}, \quad \overline{E}_{\mathrm{c}} = [(\overline{M}_{x^*\mathrm{w}} + M_{x^*\mathrm{c}})\,U]_{y^*=\delta_*}. \tag{2.10a, b}$$

Here U is the horizontal component of the mean wind, and $\tilde{u}$, u', $\tilde{v}$, and v' are the wave-induced and turbulent horizontal and vertical velocity components; P and $\tilde{p}$ are the mean and wave-induced pressures; $\tilde{r}_{ij} = \langle u_i' u_j' \rangle - \overline{u_i' u_j'}$ represent the wave-induced turbulent Reynolds stresses; ρ and δ_* are the air density and viscous-sublayer thickness; $\overline{M}_{x^*\mathrm{w}}$, $\overline{M}_{y^*\mathrm{w}}$, $\overline{E}_{x^*\mathrm{w}}$ and $\overline{E}_{y^*\mathrm{w}}$ are mean wave-supported momentum and energy fluxes, while $\overline{M}_{x^*\mathrm{c}}$, $\overline{M}_{y^*\mathrm{c}}$ and $\overline{E}_{\mathrm{c}}$ are mean momentum and energy fluxes to currents. The ratios

$$\gamma_M = \frac{\overline{M}_{x^*\mathrm{w}}}{\overline{M}_{x^*\mathrm{w}} + \overline{M}_{x^*\mathrm{c}}}, \quad \gamma_{\mathrm{E}} = \frac{\overline{E}_{\mathrm{w}}}{\overline{E}_{\mathrm{w}} + \overline{E}_{\mathrm{c}}} \tag{2.11a, b}$$

characterize the partition of momentum and energy transferred to the waves and currents.

† i.e. $< 10\,\%$ of the respective components at the fundamental mode.

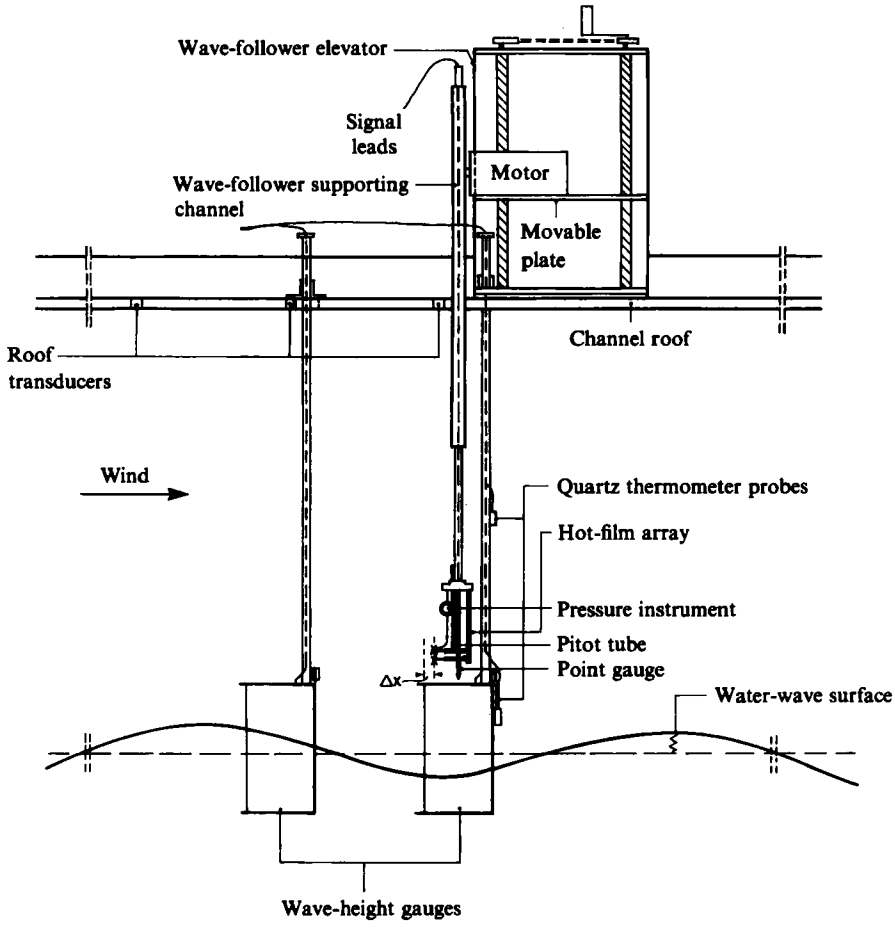

FIGURE 1. Wave-follower system and probe arrangement.

3. Experiments

3.1. *Instrumentation and calibrations*

The experiments were conducted in the Stanford wind-wave facility (see Papadimitrakis, Hsu & Street 1985*a*). The data-acquisition station was located 13 m from the air inlet. The water depth d was 0.83 m. The 1 Hz mechanically-generated wave was in deep water, with a wavelength $L = 1.56$ m and $k = 4.03$ m^{-1}.

To measure the flow in the transformed wave-following frame, the wave-follower system discussed in Papadimitrakis *et al.* (1984) was used as the primary instrument. The hot film and the wave-height gauge characteristics, their calibrations and accuracies are also described there.

The fluctuating pressure within the air boundary layer was measured with a device consisting of a thin streamlined disk, connecting tubes and a phenolic streamlined housing that contained a pressure transducer; it has been described in detail by Papadimitrakis, Hsu & Street (1986). The flattening of the central region of the disk, its circular symmetry, and the shape of the cross-section helped minimize spurious dynamic pressure variations in all three directions. In this investigation, the disk plane was set vertical and parallel to the mean air-flow direction, with the aid of an

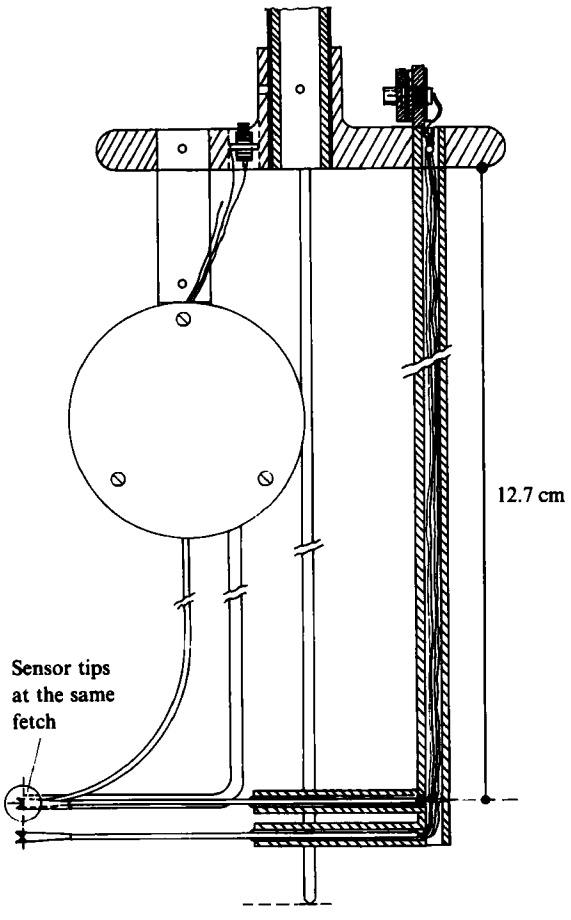

FIGURE 2. Probe arrangement close-up.

optical transit. Figure 1 shows the wave-follower system and probe arrangement, while figure 2 shows an enlargement of the latter.

All the transducers used to measure both the boundary layer and the roof pressure fluctuations were piezocrystal high-sensitivity† microphones of the 103A series made by PCB. They are ICP (integrated-circuit piezocrystal) devices featuring miniature-sized built-in solid-state electronics and acceleration compensation.

The pressure instrument and other piezocrystal transducers were calibrated dynamically against a Model P90D Pace differential transducer in a special Plexiglas chamber. The accuracy of these calibrations was about $\pm 3\%$ in amplitude and $\pm 2°$ in phase. The amplitude responses were typically flat over the frequency range 0.25–10 Hz, while the phase responses varied approximately linearly with frequency, from 0° lag at 1 Hz to 90° lag at 10 Hz. The pressure instrument was also checked *in situ* for dynamic- and mechanical-noise performance. The dynamic-noise level was found to be $\leqslant 1.5\%$ of the dynamic head for wind speed $\leqslant 5.5$ m/s, and pitch and yaw angles up to $\pm 8°$. This noise level corresponds approximately to an average signal-to-noise ratio 8:1. Further verification of the small dynamic-noise contamination of this instrument was provided by a direct comparison of its output with the

† Sensitivities varied between 1384–2650 mV/p.s.i.

pressure signal from the roof port located directly above it (Elliott 1972*a*). The spectral estimates of the two signals agreed within 24 % in amplitude and $\pm 6°$ in phase (for frequencies > 7 Hz, phase differences were larger). The mechanical noise level, defined as the RMS output pressure with the devices shielded to the corresponding unshielded value was found to be about 1 %†, and thus negligible in comparison with the over all pressure signals.

Finally the characteristics of the extraneous pressure produced by the probe motion were obtained by oscillating the pressure instrument, attached to the wave follower, in an undisturbed environment (no wind, no waves). The input to the wave follower was provided by a sinusoidal function generator. Both the amplitude and phase of the spurious pressure signal were referenced to the output signal of the wave-follower position potentiometer. At 1 Hz, the amplitude of this extraneous pressure is about 0.2 Pa, yielding an average 10:1 signal-to-noise ratio.

A detailed description of all calibration procedures along with the amplitude and phase response characteristics of both the pressure instrument and roof pressure transducers can be found in Papadimitrakis *et al.* (1985, 1986).

3.2. *Data-acquisition and reduction*

The wave height, velocity, pressure and wave-follower position potentiometer data were obtained simultaneously and recorded on digital tape for later analysis by a data-acquisition–reduction system described in Takeuchi & Mogel (1975). The hot-film and wave-follower position potentiometer signals were zero-suppressed, amplified and low-pass filtered at 250 Hz to fulfill the Nyquist criterion as samples were taken every 0.002 s for 184.32 s. The phase shifts introduced by the low-pass filters were found to be insignificant in the range 1–5 Hz, where the wave-induced velocity components are expected to be important. The pressure signals were amplified and low-pass filtered at 15 Hz; 180 blocks of 7680 digitized data points were recorded at each measurement point.

The air and water flows were permitted to settle into statistical equilibrium over a half-hour period prior to data acquisition. The velocity and pressure data were collected at 20 or 21 elevations 0.75–53.3 cm (± 0.25 mm) above the interface; they correspond to seven freestream mean wind speeds between 1.4 and 4.0 m/s.

Familiar time and phase averages were used to extract the wave-induced fluctuations from the total signals. The vertical wave-induced air velocity was corrected to account for the spurious component introduced by the wave follower motion. Cross- and autospectral analysis using $\tilde{\eta}$ as a reference were performed by fast Fourier transformation to determine the amplitude and phase of each harmonic contained in the wave-induced quantities (Hsu *et al.* 1981). The measured values of pressure amplitude and phase were corrected for frequency response of both the pressure instrument and roof transducers.

Equation (2.3) suggests that the total organized pressure contains a downstream- and an upstream-travelling wave-induced component at the fundamental mode and may have the form of a bound- and a free-travelling harmonic at higher frequencies. It also contains the spurious component produced by the oscillation of the pressure instrument inside the boundary layer and possibly sound contributions in the form of plane waves travelling upstream and downstream (Willmarth & Wooldridge 1962; Wills 1968, 1970; Latif 1974; Norris & Reynolds 1975). Thus, in our facility the

† This figure may be an overestimate of the real error, due to an apparent source of noise caused by temperature fluctuations in the air behind the films.

organized pressure waveform can consist of four components at each frequency. Separation of these periodic components utilizes their characteristic dependence upon the streamwise position in the channel. By measuring the pressure at four distinct ports along the channel roof and cross-correlating it with the wave-height gauge signal that is driving the wave follower, it is possible to resolve all the periodic components at the channel roof and isolate the acoustic contributions from the pressure measured inside the boundary layer, provided the sound waves have no vertical dependence. The resolution technique and a detailed description of the four models employed to analyse the pressure data at the channel roof, namely, the 'travelling' and 'standing' wave pressure models along with their least-squares (LS) counterparts can be found in Papadimitrakis *et al.* (1985). (Here 'travelling' and 'standing' refer to whether the acoustic pressure field is assumed to be composed of downstream- and upstream-travelling waves or of a standing wave.)

The composite sound field along with the spurious pressure due to the wave-follower motion is subtracted from the organized pressure at any measurement point. For the 'travelling' wave pressure model the amplitude p and phase $\theta_{\tilde{p}}$ of the remaining pressure at the fundamental mode can be obtained from (3.1)–(3.4), while similar expressions hold for the other pressure models and higher frequencies. Thus

$$\begin{aligned} p^2 = {} & p_{\mathrm{M}}^2 + p_{\mathrm{AI}}^2 + p_{\mathrm{AR}}^2 + p_{\mathrm{S}}^2 - 2p_{\mathrm{M}}\,p_{\mathrm{AI}}\cos(k_{\mathrm{A}}\,x^* + \theta_{\mathrm{AI}} - \theta_{\mathrm{M}}) \\ & - 2p_{\mathrm{M}}\,p_{\mathrm{AR}}\cos(k_{\mathrm{A}}\,x^* - \theta_{\mathrm{AR}} + \theta_{\mathrm{M}}) - 2p_{\mathrm{M}}\,p_{\mathrm{S}}\cos(\theta_{\mathrm{M}} - \theta_{\mathrm{S}}) \\ & + 2p_{\mathrm{AI}}\,p_{\mathrm{AR}}\cos(2k_{\mathrm{A}}\,x^* + \theta_{\mathrm{AI}} - \theta_{\mathrm{AR}}) + 2p_{\mathrm{AI}}\,p_{\mathrm{S}}\cos(k_{\mathrm{A}}\,x^* + \theta_{\mathrm{AI}} - \theta_{\mathrm{S}}) \\ & + 2p_{\mathrm{AR}}\,p_{\mathrm{S}}\cos(k_{\mathrm{A}}\,x^* - \theta_{\mathrm{AR}} + \theta_{\mathrm{S}}), \end{aligned} \tag{3.1}$$

$$\theta_{\tilde{p}} = \tan^{-1}\left(\frac{f_2}{f_1}\right)^{\circ} + \mathrm{He}(-f_1) \times 180^{\circ}, \tag{3.2}$$

where $\mathrm{He}(t)$ is the Heaviside step function and

$$f_1 = p_{\mathrm{M}}\cos\theta_{\mathrm{M}} - p_{\mathrm{AI}}\cos(k_{\mathrm{A}}\,x^* + \theta_{\mathrm{AI}}) - p_{\mathrm{AR}}\cos(k_{\mathrm{A}}\,x^* - \theta_{\mathrm{AR}}) - p_{\mathrm{S}}\cos\theta_{\mathrm{S}}, \tag{3.3}$$

$$f_2 = p_{\mathrm{M}}\sin\theta_{\mathrm{M}} - p_{\mathrm{AI}}\sin(k_{\mathrm{A}}\,x^* + \theta_{\mathrm{AI}}) + p_{\mathrm{AR}}\sin(k_{\mathrm{A}}\,x^* - \theta_{\mathrm{AR}}) - p_{\mathrm{S}}\sin\theta_{\mathrm{S}}. \tag{3.4}$$

p_{M}, θ_{M} and p_{S}, θ_{S} are the measured amplitude and phase of the organized total and spurious pressure components produced by the probe oscillation at the location (x^*, y^*); $p_{\mathrm{AI}}, \theta_{\mathrm{AI}}$ and $p_{\mathrm{AR}}, \theta_{\mathrm{AR}}$ are the corresponding quantities for the downstream- and upstream-travelling acoustic waves whose wavenumber is k_{A}. The average amplitude and phase uncertainties associated with this composite wave-induced pressure at the fundamental mode are respectively 13 % and $\pm 9°$ close to the water, and 23 % and $\pm 19°$ at the channel roof. Similar uncertainties for the corresponding channel-roof quantities were obtained for all pressure models at the higher frequencies. Since both of the wave-associated pressure components decay vertically, a two-point measurement is required to single them out within the boundary layer. Because only one pressure instrument was available off the roof, it was decided instead to treat the remaining composite wave-induced pressure as one component and recognize that the pressure associated with the reflected water wave, $\tilde{p}_{\mathrm{R}}$, may alter the true wave-induced pressure field $\tilde{p}_{\mathrm{I}}$ in the tunnel. Thus, in the air boundary layer, the term 'composite' wave-induced pressure refers to the measured periodic component of static pressure fluctuations, corrected only for instrument response and for the acoustic and the spurious wave-follower-induced contributions; this component is essentially the resultant of the two pressures associated with the downstream- and upstream-travelling water waves.

The correlations with the wave-induced pressure in the momentum and energy equations were corrected to account for frequency response of the pressure instrument and the spurious pressure components introduced by the wave-follower motion and the sound field. No attempt was made in this study to separate the spectrum of the 'reflected' and 'bound' components from the measured water-wave spectrum, although a method was developed to determine both their amplitude and phase (Papadimitrakis 1982, 1986). The results of that analysis suggest that the main wave celerity obeys the dispersion relation, if reflection effects are taken into account. At higher frequencies the presence of 'bound' and 'free' travelling components accounts for the difference between the measured and theoretical phase speeds, in agreement with the conclusions of Crawford *et al.* (1981). The presence of the wind-drift current may, of course, affect the dispersion equation, but its effect is shown to be small in a laboratory tank for the range of wind speeds examined. The average errors introduced in calculating the cross-correlations $\overline{\tilde{g}\,\partial\tilde{\eta}/\partial x^*}$, by not separating the various water-wave components, but treating them as part of the system to which the dispersion relation applies, were found to be of the order of 10 % and 4 % for the pressure- and velocity-related quantities respectively. They are relatively small, mainly because the energy of the wavetrain is concentrated at its carrier frequency, and the reflection coefficient is of the order of 5 %. No spreading factor for the directional distribution of the wind-wave field was applied to the correlations $\overline{\tilde{g}\,\partial\tilde{\eta}/\partial x^*}$, because the wind direction was assumed to be uniform and coincident with the main wave-propagating direction. Therefore

$$\overline{\tilde{p}\frac{\partial\tilde{\eta}}{\partial x^*}} = \overline{\frac{1}{c_{f'}}\tilde{p}\frac{\partial\tilde{\eta}}{\partial t^*}} = \int_0^\infty k_{f'}\,\mathrm{Qu}_{\tilde{p}\tilde{\eta}}\,\mathrm{d}f' \approx \sum_{f'_\ell}^{f'_u} k_i(f'_i)\,\mathrm{Qu}_{\tilde{p}\tilde{\eta}}(f'_i)\,\Delta f' \tag{3.5}$$

$$\overline{\tilde{p}\tilde{v}} \approx \sum_{f'_\ell}^{f'_u} \mathrm{Co}_{\tilde{p}\tilde{v}}(f'_i)\,\Delta f' \tag{3.6}$$

where $c_{f'}$ $(=g/f')$, $k_{f'}$ $(=f'^2/g)$ are the phase velocity and wavenumber at the radian frequency f'; $\mathrm{Qu}_{\tilde{p}\tilde{\eta}}$, $\mathrm{Co}_{\tilde{p}\tilde{v}}$ represent the wave-induced pressure and water-surface displacement or vertical wave-induced velocity quadrature and cospectra respectively. Similar expressions hold for the other correlations. The spectral bandwidth $\Delta f'$ and the lower and upper limits of spectral calculations, f'_ℓ and f'_u, in this study were 0.0425 Hz and 0.0425–10 Hz respectively. The average uncertainties associated with the quantities $\overline{\tilde{p}\,\partial\tilde{\eta}/\partial x^*}$ and $\overline{\tilde{p}\tilde{v}}$ were 23 % and 20 % respectively.

4. Results

Since the organized components of the sound field (at both the fundamental mode and the harmonics) and the roof wave-induced incident, reflected, bound and free pressure harmonics have been presented in Papadimitrakis *et al.* (1985), only the composite wave-induced pressure in the boundary layer (referred to hereinafter as wave-induced pressure) will be described here. This quantity appears in non-dimensional profile distributions as a function of y^*. The dynamic pressure $\frac{1}{2}\rho U_{\delta_0}^2$ and the wavenumber k are used to normalize the pressure amplitudes and y^* respectively. The wave-induced pressures are further normalized by the wave slope ka. Since $g = kc^2$ the factor $\frac{1}{2}(U_{\delta_0}/c)^2$ should be applied to these wave-induced pressure coefficients if one wishes to interpret them in terms of the quantity ρga. Here U_{δ_0} is the freestream wind speed in the core flow at the edge of the boundary layer, but it is measured conveniently at a height $\delta_0 = \frac{1}{2}H$ above the mean water level (recall that H is the depth of the air flow).

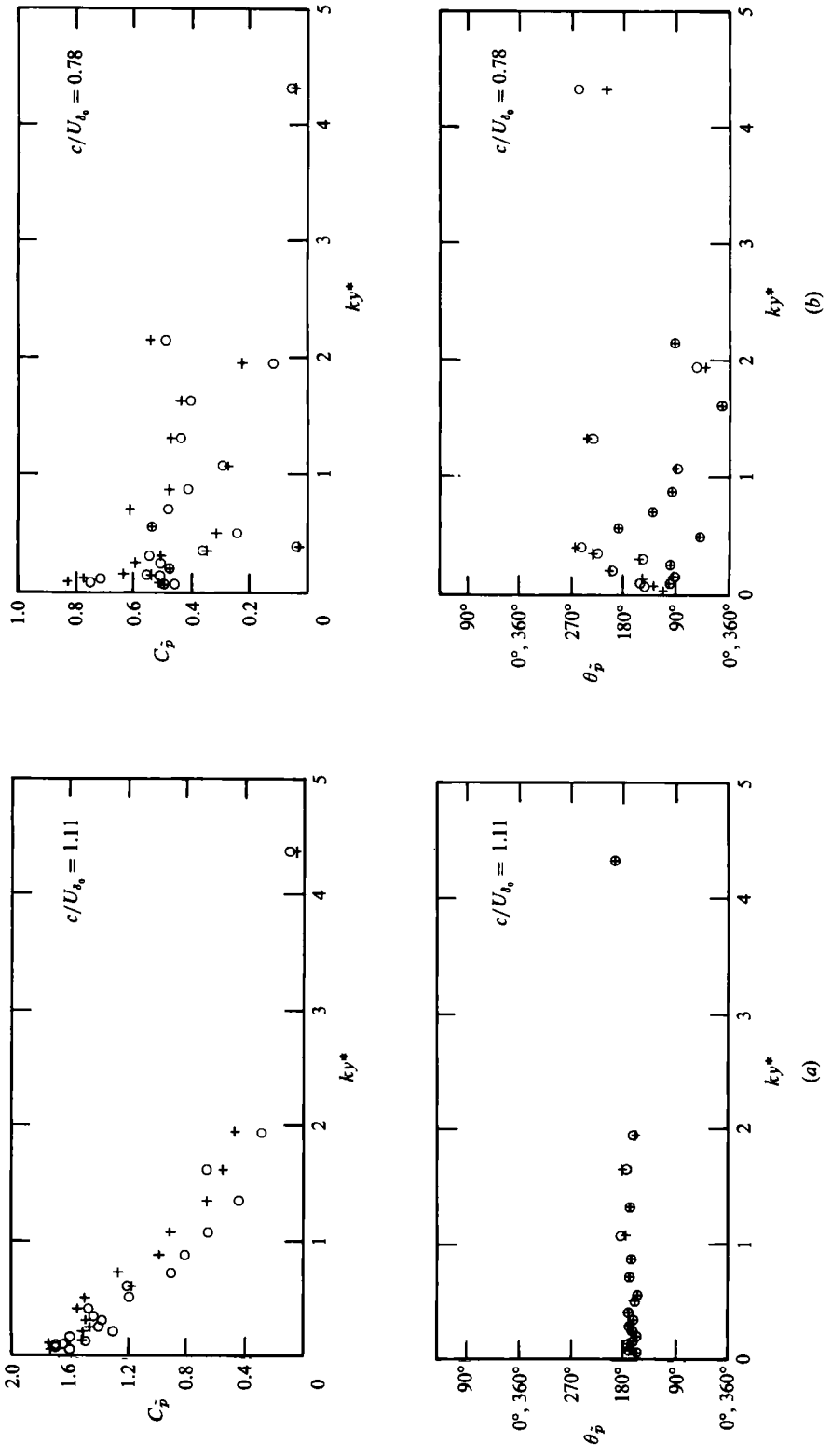

FIGURE 3 (*a*, *b*). For description see facing page.

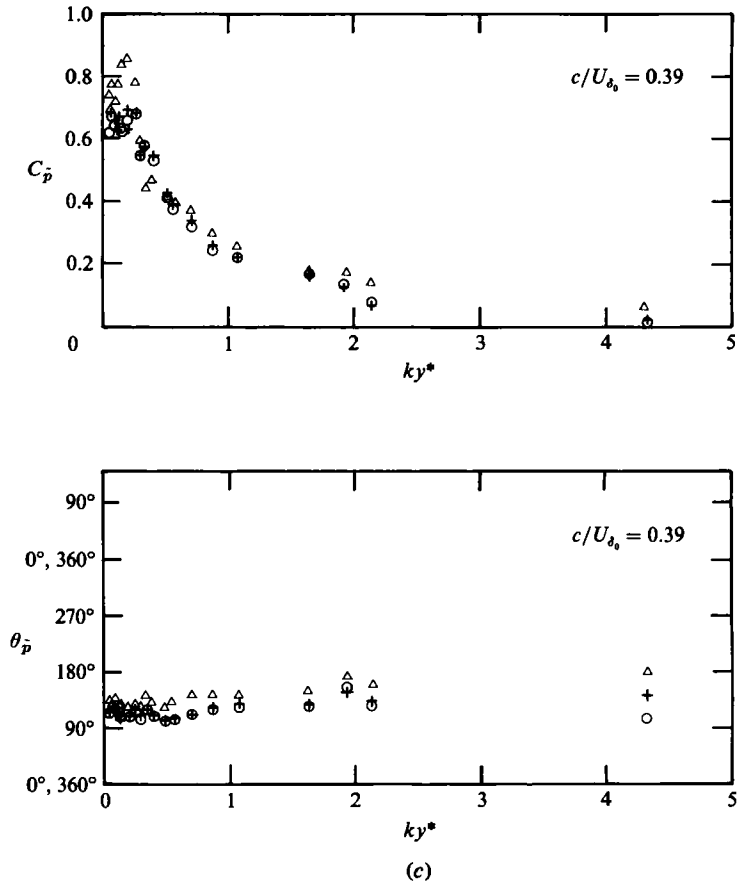

FIGURE 3. Distribution of wave-induced pressure coefficient and phase lag: ○, +, 'travelling' and LSF 'travelling' wave pressure models. △ represents the respective 'raw' quantities.

4.1. *Wave-induced boundary-layer pressure*

Figures 3(*a–c*) show the distributions of the net wave-induced pressure coefficient $C_{\tilde{p}}$ ($= 2p/ka\rho U_{\delta_0}^2$) and phase lag $\theta_{\tilde{p}}$ within the boundary layer for three typical cases. They show results deduced from both the 'travelling' wave and the LS fitting 'travelling' wave pressure models; they correspond to the fundamental water-wave frequency.

Examination of the raw pressure coefficient data (also displayed in figure 3*c*) shows that failure to account for the sound field in laboratory tanks leads to overprediction of the composite wave-induced pressure coefficient and phase lag by roughly 28 % and 20° respectively (see also §4.2, p. 128). Here the term 'raw' refers to the measured wave-induced pressure coefficients corrected only for instrument response and the spurious wave-follower-induced contributions. These results correspond to the fundamental mode at $c/U_{\delta_0} = 0.39$, but similar figures were obtained for the higher frequencies and the rest of the wind speeds studied. The acoustic contamination of the wave-induced pressure leads, in turn, to errors in the prediction of the pressure contribution to the momentum and energy exchange. The trends and qualitative conclusions to be drawn appear unaffected, however, as the comparison of our pressure data in raw and net forms indicates.

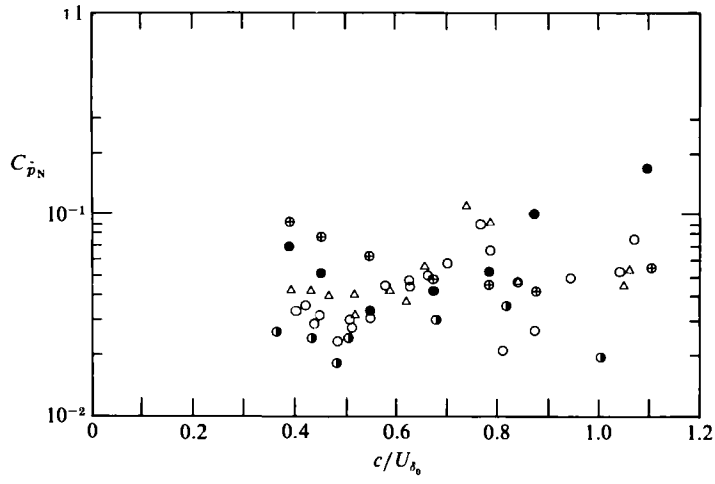

FIGURE 4. Comparison of measured wave-induced pressure amplitudes: ●, present results; ○, △, Yu & Hsu (1973); ◑, Shemdin & Hsu (1967); ⊕, potential theory.

The distribution of pressure coefficient shows an exponential decay behaviour with height, except for $c/U_{\delta_0} = 0.78$. At this wind speed both the pressure coefficient and phase lag oscillate. It has been speculated by Yu *et al.* (1973), who also observed this behaviour at $c/U_{\delta_0} = 0.81$, that the cause is flow separation. However, no evidence of flow separation was found in this study. This behaviour can be partially attributed to the higher uncertainty at this wind speed, due to the small-pressure magnitude.

A careful inspection of the velocity field at $c/U_{\delta_0} = 0.78$ reveals some interesting features of the flow at this particular wind speed (see Papadimitrakis *et al.* 1984), providing further explanation of the peculiar pressure behaviour. The stresses $\overline{\tilde{u}\tilde{u}}$ and $\overline{\tilde{u}\tilde{v}}$ have their smallest values, but they show a more regular exponential behaviour with ky^*. The small magnitude of these stresses justifies the small amplitude of the wave-induced pressure according to the analysis shown in the Appendix. The amplitudes $|\hat{r}_{11}|$ and $|\hat{r}_{22}|$, however, are considerably larger in the region $ky^* \geqslant 0.8$ for this wind speed than they are for any other wind speed. This feature may have an important implication in the distribution of the complex pressure amplitude $\hat{p}$, as shown again in the Appendix. The results of this analysis suggest that the dominant contributions to $\hat{p}$ come from the first two terms of (A 3). The first, representing the mean-shear–wave-induced-flow interaction, is similar to the potential-flow contribution, but it is respectively smaller and/or larger than the second term in the lower portion of the boundary layer and in the freestream. These two terms oscillate with phase lags varying roughly between 90° and −90° for this particular wind speed. We may therefore conclude that their combined effect results in the large amplitudes observed in the outer boundary-layer region and in the oscillatory behaviour with ky^* of both the pressure amplitude and phase. For higher or lower wind speeds, the first term in (A 3) dominates for $ky^* \geqslant 0.2$, and therefore $\hat{p}$ has a behaviour more like that of potential flow there.

A constant-pressure region close to the water surface can be discerned at the higher wind speeds, in agreement with the measurements of Yu *et al.* (1973). The general distributions of the latter, however, do not agree with ours, because their pressure coefficients increase with height, in contrast with what is expected. This increase cannot be attributed to the presence of the sound field, as can be shown by a simple

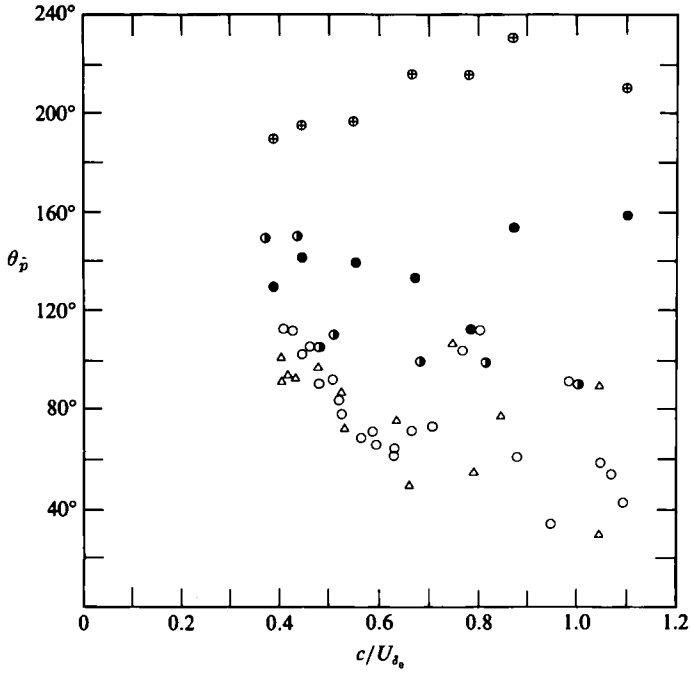

FIGURE 5. Comparison of measured wave-induced pressure phase lags; legend as in figure 4.

analysis. A systematic decrease of pressure coefficient is also observed at the two or three lowest points of measurements, and all the wind speeds considered. The above regions of constant and decreasing pressure close to the water are probably a consequence of the spatial distributions of the mean turbulent, wave-induced and wave-associated Reynolds stresses. They all show similar features in the proximity of the water and have magnitudes comparable to the term representing the mean-shear–wave-induced-field interaction in (A 3). Regions of diminishing pressure fluctuations have also been observed close to the wall in wall-bounded flows (Gibson & Launder 1978) and are known to be the consequence of 'ground' or 'wall' effects. As in wall flows, the interface suppresses the turbulent velocity fluctuations, for viscosity plays an important role there and reduces the stress and pressure magnitudes. Regions of constant pressure were also found by Townsend (1980). The distribution of the real and imaginary pressure amplitudes shown in his figure 7(*a*) bears an astonishing qualitative similarity to our distributions (figure 3), except for the case with $c/U_{\delta_0} = 0.78$. His calculations show that $p_{\text{real}} = p\cos\theta_{\tilde{p}} < 0$, provided $90° < \theta^0_{\tilde{p}} < 180°$ and $\theta_{\tilde{p}}$ is roughly constant throughout the boundary layer. The p_{imag} $(= p\sin\theta_{\tilde{p}})$ distribution also clearly shows the region of constant amplitude and the decreasing trend close to the water surface. It is therefore important to recognize these features when extrapolating pressure data to the mean or actual water surface for calculation of the transferred wind momentum, as most of the field measurements are taken high enough from the mean sea surface that they do not reveal the areas of constant and decreasing pressure regions.

For comparison of our results with previous laboratory data, the wave-induced pressure coefficient $C_{\tilde{p}_N}$ $(= 2p/\rho U^2_{\delta_0})$ and phase angles $\theta_{\tilde{p}}$ at the lowest point of measurement, plotted as functions of c/U_{δ_0}, are shown in figures 4 and 5. However, the amplitude comparison should be made with caution, as the data do not necessarily

correspond to the same measurement height for the same wind speed. It can be seen that our pressure-amplitude results fall in the range of existing data, even though the set-up and data-reduction techniques were different. The agreement between our phase results and those obtained by Yu *et al.* (1973) is rather poor. The data of Shemdin & Hsu (1967) should also be viewed with caution because of the biased reduction scheme used by them.†

The field results of Snyder *et al.* (1981) are in qualitative, and to some extent quantitative, agreement with ours, as figures 4 and 5 show, if reflection effects are taken into account. At $c/U_{\delta_0} = 0.5$ we obtain from their figure 22 that $\mathrm{Re}\,(\gamma) \approx -0.5$, $\mathrm{Arg}\,(\gamma) \approx 155°$ and $|\gamma| = 0.55$. Therefore, in our notation, $C_{\tilde{p}} \approx 0.55 \times 2(\frac{1}{2})^2 = 0.28$. From our figure 4, $C_{\tilde{p}} = C_{\tilde{p}_N}/ka \approx 0.042/0.10 \approx 0.42$. For higher wind speeds, this discrepancy among the field and laboratory data becomes smaller. Potential theory predicts that both the pressure coefficient and phase lag are affected by reflection effects and gives the following expressions for the corresponding composite quantities:

$$C_{\tilde{p}} = [C_{\tilde{p}_I}^2 + C_{\tilde{p}_R}^2 + 2C_{\tilde{p}_I} C_{\tilde{p}_R} \cos(2kx^*)]^{\frac{1}{2}}, \quad \tan\theta_{\tilde{p}} = \frac{C_{\tilde{p}_I} - C_{\tilde{p}_R}}{C_{\tilde{p}_I} + C_{\tilde{p}_I}} \tan(kx^*), \quad (4.1a, b)$$

where

$$C_{\tilde{p}_I} = 2\left(1 - \frac{c}{U_{\delta_0}}\right)^2 \frac{\cosh(k(H-y^*))}{\sinh(kH)}, \quad C_{\tilde{p}_R} = 2\epsilon\left(1 + \frac{c}{U_{\delta_0}}\right)^2 \frac{\cosh(k(H-y^*))}{\sinh(kH)}, \quad (4.2a, b)$$

with

$$\tilde{p} = p\cos(\omega t - \theta_{\tilde{p}}). \quad (4.3)$$

The same theory also predicts that $R = C_{\tilde{p}_R}/C_{\tilde{p}_I} \geqslant 1$ for $0.63 \leqslant c/U_{\delta_0} \leqslant 1.58$ and $R < 1$ for $c/U_{\delta_0} < 0.63$ or $c/U_{\delta_0} > 1.58$, provided $\epsilon \approx 0.05$. Comparison of our figure 4 with figure 22 of Snyder *et al.* yields $R \approx 0.90$ for $c/U_{\delta_0} = 0.39$ and $R \approx 6.50$ for $c/U_{\delta_0} = 1.11$. The corresponding values of R based on potential theory are 0.26 and 18 respectively. Figures 6, 7 and 9 of Snyder *et al.* also show that $\mathrm{Re}\,\gamma$ and $|\gamma|$ are not zero in the vicinity of $c/U_{\delta_0} \approx 1$, since their runs 4 and 33 may contain reflection contamination. It is now clear that our measurements reflect the influence of the travelling upwind pressures (and of the normalization with $\frac{1}{2}\rho U_{\delta_0}^2$) for $c/U_{\delta_0} > 0.63$. Potential theory, of course, does not predict any variation of R with height.

The measurements of Elliott (1972*b*), however, have suggested that

$$C'_{\tilde{p}_I} = \frac{1}{2}\left(\frac{U_{\delta_0}}{c}\right)^2 C_{\tilde{p}_I} = \exp\left[-ky^* + \alpha_1 \frac{U_{\delta_0}}{c} ky^* + \alpha_2 \frac{U_{\delta_0}}{c}\right], \quad (4.4)$$

and we may also expect that

$$C'_{\tilde{p}_R} = \frac{1}{2}\left(\frac{U_{\delta_0}}{c}\right)^2 C_{\tilde{p}_R} = \exp\left[-ky^* + a'_1 \frac{U_{\delta_0}}{c} ky^* + \alpha'_2 \frac{U_{\delta_0}}{c}\right]. \quad (4.5)$$

It can be shown through a Taylor-series expansion that the coefficient $C'_{\tilde{p}}$ can be written as

$$C'_{\tilde{p}} = \frac{1}{2}\left(\frac{U_{\delta_0}}{c}\right)^2 C_{\tilde{p}} = \exp\left[-ky^* + A_1 \frac{U_{\delta_0}}{c} ky^* + A_2 \frac{U_{\delta_0}}{c}\right]. \quad (4.6)$$

† Potential-flow theory and an average velocity (not the maximum one) were used to deduce the amplitude and phase of the wave-induced pressure. The dynamic effect of the moving probe was assumed to be in phase with the water wave, and its magnitude was determined from the recorded pressure signal at $U_{\delta_0} = c$. Their results contain also reflection contributions, but are free of sound effects owing to the referencing of the surface pressure to the freestream one.

Here $A_1 = A_1(\alpha_1, \alpha_1', U_{\delta_0}/c)$ and $A_2 = A_2(\alpha_2, \alpha_2', U_{\delta_0}/c)$. Therefore

$$R = \exp\left[(\Delta\alpha_1 ky^* + \Delta\alpha_2)\frac{U_{\delta_0}}{c}\right], \tag{4.7}$$

where $\Delta\alpha_1 = \alpha_1' - \alpha_1$ and $\Delta\alpha_2 = a_2' - \alpha_2$. Since Elliott's (1972*b*) formula is not valid outside the region $0.4 < ky^* < 2.9$, it is difficult to make inferences about $\Delta\alpha_1$ and $\Delta\alpha_2$, but we do not anticipate that $R(0, U_{\delta_0}/c) = R(kH, U_{\delta_0}/c)$. However, we suspect that the values of $R(kH, U_{\delta_0}/c)$ may increase with decreasing wind speed, as they do close to the water. Considering that the uncertainty of δR at the channel roof is roughly 30 %, we may expect values of $R(KH, U_{\delta_0}/c)$ in the range $0.55 \leqslant R \leqslant 1.55$.

The coefficients A_1 and A_2 along with their average values are shown below:

c/U_{δ_0}:	1.11,	0.87,	0.78,	0.68,	0.55,	0.45,	0.39;
A_1:	0.17,	0.27,	0.57,	0.43,	0.41,	0.16,	0.08;
A_2:	−0.38,	−0.47,	−0.76,	−0.79,	−0.84,	0.13,	0.34;

$\overline{A}_1 = 0.30$, $\overline{A}_2 = -0.40$.

These coefficients show the relative importance of reflection effects, because at high wind speeds, where reflection effects become smaller, the coefficients A_1 and A_2 approach the values obtained in the field ($\alpha_1 = 0.08$, $\alpha_2 = 0.27$). The negative values of A_2 reflect values of $C_{\tilde{p}}' < 1$ close to the water. There, potential theory does predict that for $c/U_{\delta_0} > 0.5$ and $\epsilon = 0.05$, $C_{\tilde{p}_I}'$, $C_{\tilde{p}_R}'$ and $C_{\tilde{p}}'$ are all < 1.

The pressure amplitude and phase lag, calculated according to Miles' (1957) theory, were not compared with our results, because this theory predicts only the amplitude and phase lag of the pressure component associated with the downstream-travelling water wave.

4.2. *Momentum and energy transfer*

The partition of momentum and energy between waves and currents and the contribution of the various mechanisms, viz. the wave-induced pressure, $\tilde{r}_{ij}$ and mean turbulent stresses, in transferring these quantities across the interface are now described.

Table 1 lists the coefficients γ_M, γ_E and $\gamma_{MT} = \overline{M}_w/(\overline{M}_w + \overline{M}_c)$ representing the distribution of momentum and energy partitions between waves and currents according to (2.11*a*, *b*), and the corresponding total quantities in both the x- and y-directions. Table 2 lists these quantities, along with the energy production described by the term $\overline{\tilde{u}\tilde{v}}U$. The coefficients

$$\gamma_M' = \frac{\overline{\tilde{u}\tilde{v}}}{\overline{u'v'} + \overline{\tilde{u}\tilde{v}}}, \quad \gamma_E' = \frac{(c - U_0)\,\overline{\tilde{u}\tilde{v}}}{U_0\,\overline{u'v'} + c\,\overline{\tilde{u}\tilde{v}}} \tag{4.8a, b}$$

described by Hsu *et al.* (1981) are also shown in table 1. They represent the partition of momentum and energy between waves and currents under the quasilaminar inviscid assumptions:

$$\left[\overline{\tilde{p}\frac{\partial\tilde{\eta}}{\partial x^*}}\right]_{y^*=0} = [-\rho\overline{\tilde{u}\tilde{v}}]_{y^*=0}, \quad [\overline{\tilde{p}\tilde{v}}]_{y^*=0} = [(c - U)\,\overline{\tilde{u}\tilde{v}}]_{y^*=0} \tag{4.9a, b}$$

Here $U_0\,(\approx (ka)^2 c + 0.03\,U_{\delta_0})$ represents the interfacial air velocity (Kinsman 1965; Wu 1975).

It can be seen from these tables that the momentum and energy supported by the

c/U_{δ_0}	1.11	0.87	0.78	0.68	0.55	0.45	0.39
γ_M (2.11*a*)	0.61	0.74	0.75	0.72	0.26	0.43	0.62
γ_E (2.11*b*)	0.95	0.92	0.90	0.89	0.77	0.76	0.42
γ_{MT}	0.48	0.58	0.62	0.53	0.13	0.26	0.41
γ'_M (4.8*a*)	0.80	0.65	0.45	0.78	0.46	−0.08	−0.89
γ'_E (4.8*b*)	0.95	0.93	0.90	0.93	0.87	−11.19	1.12

TABLE 1. Momentum and energy partition between waves and currents

c/U_{δ_0}	1.11	0.87	0.78	0.68	0.55	0.45	0.39
$\overline{M}_{x^*w}$	0.52×10^{-3}	1.14×10^{-3}	1.71×10^{-3}	0.80×10^{-3}	0.19×10^{-3}	0.58×10^{-3}	1.20×10^{-3}
$\overline{M}_{x^*c}$	0.33×10^{-3}	0.40×10^{-3}	0.58×10^{-3}	0.31×10^{-3}	0.54×10^{-3}	0.78×10^{-3}	0.72×10^{-3}
$\overline{M}_{y^*w}$	-0.95×10^{-5}	-1.63×10^{-5}	-1.67×10^{-5}	-1.27×10^{-5}	-1.56×10^{-5}	-1.92×10^{-5}	-2.46×10^{-5}
$\overline{M}_{y^*c}$	0.23×10^{-3}	0.41×10^{-3}	0.47×10^{-3}	0.39×10^{-3}	0.65×10^{-3}	0.89×10^{-3}	0.99×10^{-3}
$\overline{M}_w$	0.51×10^{-3}	1.11×10^{-3}	1.69×10^{-3}	0.79×10^{-3}	0.17×10^{-3}	0.56×10^{-3}	1.17×10^{-3}
$\overline{M}_c$	0.56×10^{-3}	0.81×10^{-3}	1.06×10^{-3}	0.69×10^{-3}	1.19×10^{-3}	1.68×10^{-3}	1.71×10^{-3}
$\overline{E}_w$	6.48×10^{-4}	7.05×10^{-4}	7.71×10^{-4}	3.39×10^{-4}	0.89×10^{-4}	1.51×10^{-4}	0.47×10^{-4}
$\overline{E}_c$	0.35×10^{-4}	0.60×10^{-4}	0.87×10^{-4}	0.41×10^{-4}	0.26×10^{-4}	0.47×10^{-4}	0.65×10^{-4}
$\frac{-\tilde{u}\tilde{v}U}{U^3_{\delta 0}}$	8.56×10^{-4}	5.03×10^{-4}	0.33×10^{-4}	7.28×10^{-4}	3.06×10^{-4}	-0.37×10^{-4}	-2.17×10^{-4}

TABLE 2. Momentum and energy partition between waves and currents. The transfer rates are normalized by $\rho U^2_{\delta_0}$ and $\rho U^3_{\delta_0}$, respectively.

wave form do not always represent the largest portion of the quantities transferred across the interface. It is even worse if the total momenta supported by the waves and currents (i.e. $\overline{M}_w$, $\overline{M}_c$, not $\overline{M}_{x^*w}$ and $\overline{M}_{x^*c}$) are considered.

At $c/U_{\delta_0} = 0.68$, $\gamma_M = 0.72$, $\gamma'_M = 0.78$, $\gamma_E = 0.81$, $\gamma'_E = 0.93$, $\overline{(\tilde{p}\,\partial\tilde{\eta}/\partial x^*)}/(\rho U^2_{\delta_0}) = 0.82\times10^{-3}$, $\overline{\tilde{p}\tilde{v}}/(\rho U^3_{\delta_0}) = -0.34\times10^{-3}$, $\overline{\tilde{u}\tilde{v}}/U^2_{\delta_0} = -1.09\times10^{-3}$, and $(c-U_0)\,\overline{\tilde{u}\tilde{v}}/U^3_{\delta_0} = -0.70\times10^{-3}$. At $c/U_{\delta_0} = 0.55$, $\gamma'_M = 0.46$ and $\gamma'_E = 0.87$. Thus it is not surprising that at $c/U_{\delta_0} = 0.65$ Hsu *et al.* (1981) concluded that Miles' (1957) inviscid theory may adequately describe the energy transfer from wind to waves due to the wave-induced pressure, even if there is turbulence in the wind and acoustic-pressure contributions are not accounted for by them.

The coefficients γ'_M and γ'_E do not constitute a fair representation of the actual momentum and energy partitions, as table 1 shows and consequently, Miles' (1957) inviscid quasilaminar assumptions (4.9*a*, *b*) are not always valid. At high wind speeds $\overline{\tilde{u}\tilde{v}} > 0$ and the coefficients γ'_M and γ'_E take on unrealistic values. Because various expressions for γ_E and γ_M have been used by different investigators, comparison of the relative results should be done with caution.

The difference between the present γ_M and γ_E results from those reported in Hsu *et al.* (1982) can be attributed to various reasons, such as (i) acoustic effects, (ii) the presence of mechanically generated water waves, (iii) experimental uncertainties. As mentioned earlier, the sound field contaminates the momentum- and energy-transfer calculations if not removed from pressure measurements. Comparison of the wave-induced pressure fractional contributions to the x-momentum and energy exchange (tables 2 and 4) with the corresponding calculations utilizing the (sound contaminated) 'raw' pressure data (see also §4.1, p. 123) shows that the contributions of the latter are under- or overpredicted by 18–32 % (±3–±6 %), depending on the ratio c/U_{δ_0}, with

a tendency of overprediction at high wind speeds. The dependence on c/U_{δ_0} is probably a consequence of the increased higher-frequency pressure contributions to the transfer processes at the lower wind speeds. Variations in the wave-induced pressure phase lag with both frequency and wind speed are also responsible for this wind-speed dependence. The above comparison is based in each case on one data set, and is therefore self-consistent. Our uncorrected average $\overline{\gamma}_M$ and $\overline{\gamma}_E$ coefficients (including acoustic effects) are 0.52 and 0.67 respectively. The differences between these uncorrected averages and the values $\gamma_M = 0.61$ and $\gamma_E = 0.29$ given by Hsu *et al.* (1982) lie within and outside the experimental error (± 17, $\pm 19\%$) of the raw coefficients, and can be attributed to the dissimilar dynamic conditions governing the transfer processes between wind and mechanically generated waves. The ratios c/u_* and c/D_s are $O(1)$, while for the present experiments they are $O(10)$; D_s represents the mean wind-induced surface drift current. This large current resulted in a significant leakage of the wave-supported momentum to the water currents in the experiments of Hsu *et al.* As the wind speed increases, our γ_E coefficient decreases, as it should, as a result of the decreasing ratio c/D_s and the increasing leakage of the wave-supported momentum to currents. Part of the differences may be also attributed to the different fetches being used in both experiments. As shown in Papadimitrakis (1982) and further elaborated in Papidimitrakis (1986), the effect of the mean drift current on the dispersion relation is negligible for low wind speeds ($c/U_{\delta_0} > 0.5$, say) and small for $c/U_{\delta_0} < 0.5$. However, the cumulative error made in the calculation of γ_M and γ_E by neglecting water current, reflection and bound component effects on the dispersion relation, remains more or less constant and $O(10\%)$. At low wind speeds the error associated with bound component effect dominates, because of the increased contributions to the $\overline{\tilde{p}\,\partial\tilde{n}/\partial x^*}$ cross-correlation from higher-frequency pressure components. At higher wind speeds the contributions from higher frequencies become smaller, and the error associated with water-current effects becomes larger. The above combined error results in a 3% increase of the originally estimated 10% uncertainty for the quantity $\overline{\tilde{p}\,\partial\tilde{n}/\partial x^*}$.

Snyder *et al.* (1981) reported similar values of the momentum transfer to the waves as a fraction of sonic stress. Their γ_M coefficient ranged between 0.20–0.91, depending on the wind speed. Our experimental results yielded values 0.20–0.72 for γ_M and 0.40–0.92 for γ_E. For the wind speeds examined in this study, the dimensionless fetch $\tilde{x} = xg/u_*^2$ varies between 6.24×10^4 and 4.66×10^3. Comparison of γ_M values and those of Snyder *et al.* (1981) shows that our γ_M are larger at small and moderate wind speeds ($c/U_{\delta_0} \geqslant 0.68$), corresponding to large and moderate dimensionless fetches. This is anticipated, however, because in this region the reflection pressures dominate the transfer processes in our experiments ($R \gg 1$). For $c/U_{\delta_0} \approx 0.55$, where $\tilde{x} = 1.88 \times 10^4$ and there is evidence that the incident wave-induced pressure is at least equal to the reflected one, our γ_M coefficient is 0.26, as opposed to the value $\gamma_M = 0.20$ of Snyder *et al.*, corresponding to $c/U_{\delta_0} = 0.57$ and a dimensionless fetch $\tilde{x} \approx 10^4$. For $c/U_{\delta_0} \leqslant 0.5$ our γ_M values increase with wind speed, as they should, provided $\tilde{x}$ decreases.

From the above discussion it is evident that, aside from reflection effects and the presence of pressure harmonics, there is a remarkable similarity between laboratory and field wave-induced pressures and therefore between the corresponding governing transfer processes for the same range of dimensionless wind speed c/U_{δ_0} and $\tilde{x}$, when a long mechanically generated water-wave train is present, provided acoustic effects have been properly accounted for in laboratory measurements.

Table 3 lists the fractional contribution of the wave-induced pressure and other

c/U_{δ_0}	1.11	0.87	0.78	0.68	0.55	0.45	0.39
$\overline{\tilde{p}\dfrac{\partial\tilde{\eta}}{\partial x^*}}\Big/\overline{M}_{x^*\mathrm{w}}$	0.952	0.989	1.019	1.019	1.135	1.064	1.040
$\overline{\tilde{p}\dfrac{\partial\tilde{\eta}}{\partial x^*}}\Big/\overline{M}_{\mathrm{w}}$	0.970	1.004	1.029	1.036	1.239	1.100	1.061
$\overline{\rho\tilde{r}_{11}\dfrac{\partial\tilde{\eta}}{\partial x^*}}\Big/\overline{M}_{\mathrm{w}}$	0.050	−0.002	−0.019	−0.020	−0.150	−0.066	−0.040
$\overline{-\tilde{r}_{12}\dfrac{\partial\tilde{\eta}}{\partial x^*}}\Big/\overline{M}_{\mathrm{w}}$	−0.020	−0.002	−0.010	0.016	−0.089	−0.034	−0.021
$\overline{\tilde{p}\tilde{v}}/\overline{E}_{\mathrm{w}}$	0.995	1.000	1.001	0.994	0.994	1.000	0.976
$-\rho\overline{\tilde{r}_{12}\tilde{u}}/\overline{E}_{\mathrm{w}}$	−0.005	0.000	−0.003	−0.019	−0.119	−0.092	−0.265
$-\rho\overline{\tilde{r}_{22}\tilde{v}}/\overline{E}_{\mathrm{w}}$	0.002	0.000	−0.002	−0.002	−0.089	0.000	0.030
$\rho(\overline{u'u'}-\overline{v'v'})\overline{\dfrac{\partial\tilde{\eta}}{\partial x^*}\tilde{u}}\Big/\overline{E}_{\mathrm{w}}$	0.006	0.000	0.004	0.026	0.130	0.092	0.241
$\rho\,\overline{u'v'}\,\overline{\dfrac{\partial\tilde{\eta}}{\partial x^*}\tilde{v}}\Big/\overline{E}_{\mathrm{w}}$	0.002	0.000	0.000	0.001	0.040	0.000	−0.030

TABLE 3. Fractional contributions of the various mechanisms to the momentum and energy transfers supported by the waves

c/U_{δ_0}	1.11	0.87	0.78	0.68	0.55	0.45	0.39
$\overline{\tilde{p}\dfrac{\partial\tilde{\eta}}{\partial x^*}}$	58.37 %	73.29 %	75.92 %	73.71 %	29.53 %	45.24 %	64.87 %
$\overline{\rho\tilde{r}_{11}\dfrac{\partial\tilde{\eta}}{\partial x^*}}$	2.91	0.77	−1.38	−1.45	−3.57	−1.73	−2.52
$-\rho\,\overline{u'v'}$	38.72	25.94	25.46	27.74	74.04	57.49	37.65
$\overline{M}_{x^*}$	100	100	100	100	100	100	100
$-\overline{\tilde{p}\tilde{v}}$	94.37	92.17	89.88	88.67	76.76	76.20	40.44
$-\rho\overline{\tilde{r}_{22}\tilde{v}}$	−0.48	−0.48	−0.32	−1.73	−9.20	−7.00	−11.00
$-\rho\overline{\tilde{r}_{12}\tilde{u}}$	0.17	−0.11	−0.24	−0.22	−0.69	−0.25	0.14
$\rho(\overline{u'u'}-\overline{v'v'})\overline{\dfrac{\partial\tilde{\eta}}{\partial x^*}\tilde{u}}$	0.63	0.46	0.39	0.35	10.04	7.01	11.96
$\rho\,\overline{u'v'}\,\overline{\dfrac{\partial\tilde{\eta}}{\partial x^*}\tilde{v}}$	0.17	0.13	0.11	0.12	0.29	0.11	−0.08
$\overline{E}_{\mathrm{c}}$	5.14	7.83	10.18	10.81	22.8	23.93	58.43
$\overline{E}_{\mathrm{T}}$	100	100	100	100	100	100	100

TABLE 4. Fractional contributions of various mechanisms to x-momentum and total energy exchange

mechanisms to the momentum and energy supported by the waves. The contribution to currents by the mean pressure has not been included. For large dimensionless fetch $\tilde{x}$, 16–20 % of the wave-supported momentum $\overline{M}_{x^*_w}$ comes from pressure contributions at higher frequencies† and mainly from 4 Hz. However, these contributions do not decrease monotonically with increasing c/U_{δ_0}, as table 10 of Snyder *et al.* (1981) shows. This result is not totally consistent with the observations of Snyder *et al.* and Hsu *et al.* (1982). The former have found that the higher frequencies ($\tilde{\omega} > 3$ in their notation) contribute mainly to the momentum transfer, whereas the experiments of the latter indicated that the higher frequencies have a negligible contribution and that the fundamental wave mode receives most of the wind energy (and, therefore, of momentum) input. The mixed behaviour observed in our experiments probably reflects the presence of bound pressure harmonics, as well as the only partially similar physical and dynamical field and laboratory conditions‡ in the presence of mechanically generated water waves.

The results of table 3 show that under the present experimental conditions the wave-induced pressure dominates the transfers supported by the wave form, because the wave-induced and turbulent stresses have negligible contribution. However, they are significant in the transport processes, because they indirectly distort the undulating critical layer and therefore affect the behaviour of the wave-induced pressure. The ratios $\overline{\tilde{p}(\partial\tilde{\eta}/\partial x^*)}/\overline{M}_{x^*_w}$ and $\overline{\tilde{p}\tilde{v}}/\overline{E}_w$ may even exceed unity because of possible negative contributions of the other mechanisms. Table 4 shows the fractional contribution of the same mechanisms to the x-momentum and total energy exchange. The wave-induced pressure contributes about 98–124 % to the total wave-supported momentum and 98–100 % to the wave-supported energy. Its contribution to the total momentum and energy transferred across the interface, however, is much smaller because of the significant contribution of the mean turbulent stresses to currents. The wave-induced pressure contributes also to the energy transferred to currents. Thus, to summarize, the wave-induced pressure plays a significant role in transferring momentum and energy to the waves (it is almost *the* exclusive transferring mechanism), but does not always dominate in the transfer of total momentum and energy to both waves and currents.

The dominance of the wave-induced pressures in the transfer process was also observed by Hsu *et al.* (1982), although they did not account for acoustic effects. While the sound contribution amounts to $< 32\,\%$ of the uncorrected $\tilde{p}\,\overline{\partial\tilde{\eta}/\partial x^*}$ and $\overline{\tilde{p}\tilde{v}}$ quantities, the $\tilde{r}_{ij}$ contribution is negligible. Although in their experiments the wave-induced Reynolds stresses contribute 27 and $-67\,\%$ of the wave-supported momentum and energy, the respective wave-induced pressure contributions amount to 73 and 167 %, and therefore acoustic effects do not alter the predominant character of the wave-induced pressure in their measurements. The negligible contribution of the $\tilde{r}_{ij}$ stresses to the transfer processes observed in our experiments is again the result of turbulence suppression in the presence of mechanically generated long waves. Thus our ratios $\overline{\tilde{p}(\partial\tilde{\eta}/\partial x^*)}/\overline{M}_{x^*_w}$ and $\overline{\tilde{p}\tilde{v}}/\overline{E}_w$ remain practically unaltered by the sound field, and their conclusion is qualitatively justified.

For $c/U_{\delta_0} = 0.39$ our measurements yielded $\overline{\tilde{p}\tilde{v}}/(-\overline{\tilde{u}\tilde{v}}U) = 0.21$, at the lowest

† i.e. in approximate form from the term: $\sum_{i=2}^{5} \tilde{p}_i\,\partial\tilde{\eta}_i/\partial x^*$; the subscript refers to pressure and water-wave harmonics.

‡ As expressed by the parameters c/u_* and $\tilde{x}$.

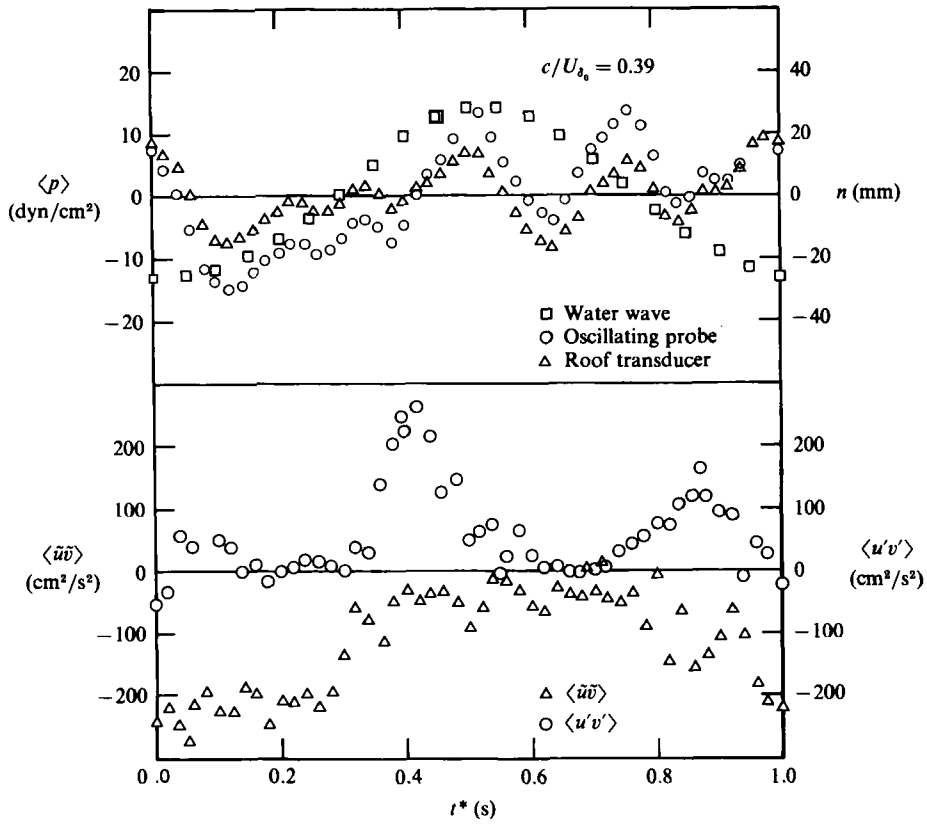

FIGURE 6. Phase-averaged results of pressure, wave-associated and turbulent Reynolds stresses (after Papadimitrakis *et al.* 1985*a*).

point of measurements, close to the value 0.1 reported by Elliott (1972*b*). Thus for this particular wind speed the $\overline{\tilde{p}\tilde{v}}$ correlation is small compared with the energy production, as Lumley & Panofsky (1964) suggested.

5. Discussion of wave-induced pressure behaviour

The typical phase-averaged pressure results shown in figure 6 and also presented in Papadimitrakis *et al.* (1985) revealed the existence of rather strong wave-induced pressure harmonics, in contrast with field behaviour and the behaviour of the wave-induced velocities. Of course, the pressure is a nonlinear function of the velocity field, as (A 3) suggests. This equation clearly shows the contributions of the wave–wave interactions to the wave-induced pressure. The phase-averaged $\langle \tilde{u}\tilde{v} \rangle$ results shown in figure 6 demonstrate the importance of at least one of the nonlinear terms contributing to the wave-induced pressure field. Corcos (1964) is also of the opinion that these nonlinear terms may be of importance. The small $\langle \tilde{u}\tilde{v} \rangle$ and $\langle u'v' \rangle$ harmonics may give rise to pressure fluctuations, which then interact with each other and the wave-induced pressure component at the fundamental mode to produce stronger harmonics.

Further evidence for the nonlinear behaviour of the wave-induced pressure field may be the presence of the bound pressure harmonics found in our experiments. Gent

& Taylor (1976) and Gent (1977) reported significant variations in their predicted wave-induced surface-pressure distributions with the wave slope, but no double peaks were found by them. However, they have also pointed out that for $ka > 0.05$ the nonlinearities of water surface become important. Wave–wave second-order resonant interactions among a set of three wave modes that does not precisely satisfy the resonance conditions or other mechanisms may also be responsible for the presence of strong pressure harmonics, as Phillips (1977, pp. 31, 111) has shown.

The nonlinear behaviour of the wave-induced pressure field manifested itself with a slight variation of its own amplitude with time, as equation (2.8.2) in Phillips (1977, p. 28) shows. This behaviour was observed in our channel-roof pressure data, where the amplitude of the organized pressure component showed slight variations during the traversing of the boundary layer.

As discussed previously, the presence of strong wave-induced pressure harmonics has some influence on the wave-supported momentum $\overline{M}_{x^*_{\mathrm{w}}}$. The contribution of these harmonics to $\overline{M}_{x^*_{\mathrm{w}}}$ (about (0.16–0.2) $\overline{M}_{x^*_{\mathrm{w}}}$) is different from either field or previous laboratory results, as it is neither dominant nor totally insignificant in the transfer processes. However, because it is the total pressure contribution ($\approx \sum_{i=1}^{5} \tilde{p}_i \partial \tilde{n}_i / \partial x^*$) that determines γ_M, and this contribution depends on $\tilde{x}$, exact comparison of field and laboratory results becomes difficult, owing to the lack of identical ($\tilde{x}$) conditions. Therefore, for laboratory-data, conclusions regarding the influence of the wave-induced pressure harmonics on γ_M are difficult to make, at least before multiple fetch measurements (in the transformed coordinate system) are available and the effects of fetch on the development of these harmonics are known. Further work on the behaviour of the wave-induced pressures found in our experiments and their possible effects on the wave-generation processes is being currently conducted, and will be reported separately.

6. Summary and conclusions

A set of experiments was conducted to study the behaviour of the wave-induced pressure over 1 Hz small-amplitude mechanically generated water waves, in order to evaluate its contribution to the momentum and energy exchange. Based on the results and the discussions presented in §§4 and 5, the following conclusions can be drawn.

(i) Neglecting the acoustic contamination of the organized static pressure fluctuation leads to errors in the prediction of the amplitude and phase lag of the wave-induced pressure by approximately 28 % and 20°, and in its contribution to the momentum and energy exchange between 18–32 %, depending on the ratio c/U_{δ_0}. However, the contamination does not appear to alter the trends and qualitative conclusions presented for example in Hsu *et al.* (1982).

(ii) The fundamental mode of the wave-induced pressure decays exponentially with height inside the boundary layer, but the rate of decay is different from that predicted by potential-flow theory. At low and moderate wind speeds ($c/U_{\delta_0} > 0.63$†), the pressure caused by reflected waves dominates, and a significant change in the pressure distribution is expected. The rate of pressure decay with height is much greater than predicted by potential theory in this case. At higher wind speeds ($c/U_{\delta_0} < 0.63$) the downwind pressures are expected to be of equal or greater importance than the reflected ones, and the above distributions return progressively

† This value depends on the reflection coefficient (see Papadimitrakis *et al.* 1985).

to forms comparable to their field data counterparts. At high enough wind speeds (say $c/U_{\delta_0} < 0.45$, where reflection effects become small), the decay rate is smaller than predicted by potential theory, in agreement with Elliott's (1972*b*) field observations. Thus, while potential theory, depending on the ratio c/U_{δ_0}, either over- or underestimates the wave-induced pressure amplitudes and phase lags measured in a wave tank, Miles' (1957) theory cannot be compared with laboratory results because of the presence of upwind-travelling wave-induced pressures.

(iii) The phase lag between the wave-induced pressure and water waves remains fairly constant throughout the boundary layer, except at $c/U_{\delta_0} = 0.78$ and 0.68, where both the pressure amplitude and phase lag fluctuate. This phase difference depends on the ratio c/U_{δ_0}, and it is not constant. For active wave generation it is approximately 130°, with the pressure lagging waves.

(iv) The momentum and energy transport processes are wind-field-dependent. The wave-induced pressure dominates the wave-supported momentum and energy transfer rates. However, it does not always dominate the transfer of the corresponding total quantities to both waves and currents and may contribute significantly to the energy transferred into currents, depending on the ratio c/U_{δ_0}. The wave-induced Reynolds stresses make only a small direct contribution. The mean shear stress contributes significantly to the momentum and energy transfer directly into currents. The partition γ_M and γ_E of momentum and energy between waves and currents found in this investigation varies between 0.26–0.75 and 0.42–0.95 respectively, depending on the ratio c/U_{δ_0}. For low and moderate wind speeds, the coefficient γ_M is larger than its field value for the same dimensionless fetch, owing to the reflected pressures. For high wind speeds the field and laboratory values of γ_M are comparable. However, because the pressure associated with the reflected wave, $\tilde{p}_{\mathrm{R}}$, was found to be significant at the channel roof (Papadimitrakis *et al.* 1985), interpretations regarding the importance of the true wave-induced pressure $\tilde{p}_{\mathrm{I}}$ in the transfer of wind momentum to water waves in laboratory studies should be made with caution, as long as $\tilde{p}_{\mathrm{R}}$ remains in boundary-layer measurements of the wave-induced pressure in wind-wave facilities.

The authors are grateful to the referees for their invaluable comments and suggestions. This work was supported mainly by the National Science Foundation through grant NSF-CEE-7817618. One of us (R. L. S.) has also received support from the Office of Naval Research under contract N00014-84-K-0242.

Appendix

The x^* momentum equation in the transformed coordinate system (equation (2.67) in Papadimitrakis 1982) solved for $\hat{p}^*$ yields

$$\hat{p}^* = \frac{1}{\mathrm{i}k}\left[(U-c)\,\mathrm{D}\hat{v}^* - \hat{v}^*\mathrm{D}^*U + \nu \mathrm{i}k^{-1}(\mathrm{D}^{*3} - k^2\mathrm{D}^*)\,\hat{v}^* - \mathrm{i}k\hat{r}^*_{11} - \mathrm{D}^*\hat{r}^*_{12} - \mathrm{i}k\hat{w}^*_{11} - \mathrm{D}^*\hat{w}^*_{12}\right], \tag{A 1}$$

where $\hat{}$ denotes complex amplitude, $\mathrm{D}^* = \mathrm{d}/\mathrm{d}y^* = \mathrm{D}$, $\mathrm{i} = \sqrt{(-1)}$ and the pressure has been normalized by the air density;

$$\hat{v}^* = \hat{v}, \quad \hat{p}^* = \hat{p} - fa\frac{\partial P}{\partial y^*}, \quad \hat{r}^*_{ij} = \hat{r}_{ij} - fa\frac{\partial(\overline{u'_i u'_j})}{\partial y^*},$$

$$\hat{w}^*_{ij} = \hat{w}_{ij} - fa\frac{\partial(\overline{\tilde{u}_i \tilde{u}_j})}{\partial y^*}, \quad \tilde{w}_{ij} = \langle \tilde{u}_i \tilde{u}_j \rangle - \overline{\tilde{u}_i \tilde{u}_j},$$

and f is given by (2.4). Since the mean pressure remains roughly constant within the air boundary layer and viscosity is unimportant away from the interface, we can write

$$\hat{p} \approx \frac{1}{\mathrm{i}k}\left[(U-c)\,\mathrm{D}\hat{v} - \hat{v}\mathrm{D}U - \mathrm{i}k(\hat{r}_{11}+\hat{w}_{11}) + \mathrm{i}(ka)f\mathrm{D}(\overline{u'^2}+\overline{\tilde{u}^2})\right.$$
$$\left. - \mathrm{D}(\hat{r}_{12}+\hat{w}_{12}) + a\mathrm{D}f\,\mathrm{D}(\overline{u'v'}+\overline{\tilde{u}\tilde{v}}) + af\mathrm{D}^2(\overline{u'v'}+\overline{\tilde{u}\tilde{v}})\right]. \quad \text{(A 2)}$$

The stresses $\langle \tilde{u}_i \tilde{u}_j \rangle$ have their main component at 2 Hz (see Papadimitrakis *et al.* 1984) and make no significant contribution to the fundamental pressure mode; therefore

$$\tilde{p} \approx \frac{1}{\mathrm{i}k}\left[\underbrace{(U-c)\,\mathrm{D}\hat{v}-\hat{v}\mathrm{D}U}_{(1)} - \underbrace{\mathrm{i}k\hat{r}_{11}}_{(2)} - \underbrace{\mathrm{D}\hat{r}_{12}}_{(3)} + \underbrace{\mathrm{i}(ka)f\mathrm{D}(\overline{u'^2}+\overline{\tilde{u}^2}}_{(4)}\right.$$
$$\left. + \underbrace{a\mathrm{D}f\mathrm{D}(\overline{u'v'}+\overline{\tilde{u}\tilde{v}})}_{(5)} + \underbrace{af\mathrm{D}^2(\overline{u'v'}+\overline{\tilde{u}\tilde{v}})}_{(6)}\right]. \quad \text{(A 3)}$$

We can now obtain an estimate of the various terms (1)–(6) in the above expression for $ky^* \geqslant 0.2$, utilizing the available information from our velocity measurements; $\tilde{v}$ can be approximated as $\tilde{v} = (U-c)f\partial\tilde{\eta}/\partial x^*$, and therefore $\hat{v} \approx kaf(U-c)$. Hsu & Hsu (1983) showed that this expression yields reliable results even close to the water surface. First, $\hat{p}_1 = (U-c)\,\mathrm{D}\hat{v} - \hat{v}\mathrm{D}U \approx k(ka)f(U-c)^2$, provided f approaches e^{-ky^*} for large H; $\hat{p}_{1\mathrm{N}} = \hat{p}_1/U_{\delta_0}^2 = kaf[(U-c)/U_{\delta_0}]^2$. From the mean-stress distributions, it is also evident that $\mathrm{D}\overline{\tilde{u}^2} \ll \mathrm{D}\overline{u'^2}$ in the region under consideration; $\mathrm{D}\overline{u'^2} \sim -400$, $\hat{p}_4 = \mathrm{i}kaf\mathrm{D}(\overline{u'^2}+\overline{\tilde{u}^2}) \sim \mathrm{i}kaf\mathrm{D}\overline{u'^2}$ and $\hat{p}_{4\mathrm{N}} = \hat{p}_4/U_{\delta_0}^2 \sim -\mathrm{i}f\times 10^{-3}$.

The stress $-\overline{u'v'}$ has an almost-constant slope in the region $ky^* \geqslant 0.2$, except probably in the freestream, where this slope approaches zero. The contribution of the $\mathrm{D}\overline{\tilde{u}\tilde{v}}$ term is negligible and, since $\mathrm{D}f \approx -kf$, the fifth term becomes

$$\hat{p}_{5\mathrm{N}} = \frac{a\mathrm{D}f\,\mathrm{D}(\overline{u'v'}+\overline{\tilde{u}\tilde{v}})}{U_{\delta_0}^2} \approx -\frac{kaf\mathrm{D}(\overline{u'v'})}{U_{\delta_0}^2} = 1.5f.$$

The contribution of the sixth term is also negligible for $ky \geqslant 0.2$, because $\mathrm{D}^2(\overline{u'v'}+\overline{\tilde{u}\tilde{v}}) \approx 0$ there. Average magnitudes of the various normalized terms contributing to the wave-induced pressure are given below:

$$\hat{p}_{1\mathrm{N}} = 19, \quad \hat{p}_{2\mathrm{N}} = 15, \quad \hat{p}_{3\mathrm{N}} = 5, \quad \hat{p}_{4\mathrm{N}} = 4, \quad \hat{p}_{5\mathrm{N}} = 0.6, \quad \hat{p}_{6\mathrm{N}} \approx 0.$$

REFERENCES

Corcos, G. J. 1964 The structure of the turbulent pressure field in boundary layer flows. *J. Fluid Mech.* **18**, 353.

Crawford, D. R., Lake, B. M., Saffman, P. G. & Yuen, H. C. 1981 Effects of nonlinearity and spectral bandwidth on the dispersion relation and component phase speeds of surface gravity waves. *J. Fluid Mech.* **112**, 1.

Dobson, F. W. 1971 Measurements of atmospheric pressure on wind-generated sea waves. *J. Fluid Mech.* **48**, 91.

Elliott, J. A. 1972*a* Microscale pressure fluctuations measured within the lower atmospheric boundary layer. *J. Fluid Mech.* **53**, 351.

Elliott, J. A. 1972*b* Microscale pressure fluctuations near waves being generated by the wind. *J. Fluid Mech.* **54**, 427.

Garrett, G. R. L. 1970 On cross-waves. *J. Fluid Mech.* **41**, 837.

GENT, P. R. 1977 A numerical model of the air flow above water waves. Part 2. *J. Fluid Mech.* **82**, 349.

GENT, P. R. & TAYLOR, P. A. 1976 A numerical model of air flow above water waves. *J. Fluid Mech.* **77**, 105.

GIBSON, M. M. & LAUNDER, B. E. 1978 Ground effects on pressure fluctuations in the atmospheric boundary layer. *J. Fluid Mech.* **86**, 491.

HSU, C. T. & HSU, E. Y. 1983 On the structure of turbulent flow over progressive water waves: theory and experiment in a transformed coordinate system. Part 2. *J. Fluid Mech.* **131**, 123.

HSU, C. T., HSU, E. Y. & STREET, R. L. 1981 On the structure of turbulent flow over a progressive water wave: theory and experiments in a transformed wave-following coordinate system. Part 1. *J. Fluid Mech.* **105**, 87.

HSU, C. T., WU, H. Y., HSU, E. Y. & STREET, R. L. 1982 Momentum and energy transfer in wind generation of waves. *J. Phys. Oceanogr.* **12**, 929.

HSU, E. Y. 1965 A wind, water-wave research facility. *Civil Engng Dept Rep.* 57, *Stanford University.*

KINSMAN, B. 1965 *Wind Waves: Their Generation and Propagation on the Ocean Surface.* Prentice-Hall.

LAKE, B. M. & YUEN, H. C. 1978 A new model for nonlinear waves. Part 1. Physical model and experimental evidence. *J. Fluid Mech.* **88**, 33.

LATIF, A. M. 1974 Acoustic effects on pressure measurements over water waves in the laboratory. Ph.D. dissertation, University of Florida.

LUMLEY, J. L. & PANOFSKY, H. A. 1964 *The Structure of Atmospheric Turbulence.* Interscience.

MADSEN, O. S. 1971 On the generation of long waves. *J. Geophy. Res.* **76**, 8672.

MILES, J. W. 1957 On the generation of surface waves by shear flows. *J. Fluid Mech.* **3**, 185.

NORRIS, H. L. & REYNOLDS, W. C. 1975 Turbulent channel flow with a moving wavy boundary. *Mech. Engng Dept Rep.* TF-7, *Stanford University.*

PAPADIMITRAKIS, Y. A. 1982 Velocity and pressure measurements in the turbulent boundary layer above mechanically-generated water waves. Ph.D. dissertation, Civil Engineering Department, Stanford University.

PAPADIMITRAKIS, Y. A. 1986 On the structure of artificially-generated water wave trains. *J. Geophys. Res.* (to appear).

PAPADIMITRAKIS, Y. A., HSU, E. Y. & STREET, R. L. 1984 On the structure of the velocity field over progressive, mechanically-generated water waves. *J. Phys. Oceanogr.* **14**, 1937.

PAPADIMITRAKIS, Y. A., HSU, E. Y. & STREET, R. L. 1985 On the resolution of spurious pressure fluctuations in wind-wave facilities. *J. Acoust. Soc. Am.* **77**, 896.

PAPADIMITRAKIS, Y. A., HSU, E. Y. & STREET, R. L. 1986 Instrument for measuring turbulent pressure fluctuations. *Rev. Sci. Instrum.* **57**, 666.

PHILLIPS, O. M. 1977 *The Dynamics of the Upper Ocean.* Cambridge University Press.

PHILLIPS, O. M. & BANNER, M. L. 1974 Wave breaking in the presence of wind drift and swell. *J. Fluid Mech.* **66**, 625.

SHEMDIN, O. H. & HSU, E. Y. 1967 Direct measurements of aerodynamic pressure above a simple progressive gravity wave. *J. Fluid Mech.* **30**, 403.

SNYDER, R. L. 1974 A field study of wave-induced pressure fluctuations above surface gravity waves. *J. Mar. Res.* **32**, 497.

SNYDER, R. L., DOBSON, F. W., ELLIOTT, J. A. & LONG, R. B. 1981 Array measurements of atmospheric pressure fluctuations above surface gravity waves. *J. Fluid Mech.* **102**, 1.

TAKEUCHI, K. & MOGEL, T. R. 1975 A performance evaluation of a mini-computer. *Rev. Sci. Instrum.* **46**, 686.

TOWNSEND, A. A. 1980 The response of sheared turbulence to additional distortion. *J. Fluid Mech.* **81**, 171.

WILLMARTH, W. W. & WOOLDRIDGE, C. E. 1962 Measurements of the fluctuating pressure on the wall beneath a thick turbulent boundary layer. *J. Fluid Mech.* **14**, 187.

WILLS, J. A. B. 1968 Spurious pressure fluctuations in wind tunnels. *J. Acoust. Soc. Am.* **43**, 1049.

WILLS, J. A. B. 1970 Measurements of the wave-number/phase velocity spectrum of wall pressure beneath a turbulent boundary layer. *J. Fluid Mech.* **45**, 65.

WU, H. Y., HSU, E. Y. & STREET, R. L. 1979 Experimental study of nonlinear wave–wave interaction and whitecap dissipation on wind-generated waves. *Dyn. Atmos. Oceans* **3**, 55.

WU, J. 1975 Wind-induced drift currents. *J. Fluid Mech.* **68**, 49.

YU, H. Y., HSU, E. Y. & STREET, R. L. 1973 A refined measurement of aerodynamic pressure over progressive water waves. *Civil Engng Dept Rep.* 146, *Stanford University*.